Orbital-scale global ocean sea surface temperatures coupling with cryosphere-carbon cycle changes over the past 4 million years

Ze Zhang[1], Eelco J. Rohling[2,3], David B. Kemp[4], Zhixiang Wang[5*], Chunju Huang[4*]

[1]Department of Atmospheric Science, School of Environmental Studies, China University of Geosciences, Wuhan 430074, China

[2]Department of Earth Sciences, Utrecht University, Princetonlaan 8, 3584 CB Utrecht, The Netherlands

[3]Ocean and Earth Science, University of Southampton, National Oceanography Centre, Southampton, SO14 3ZH, UK

[4]State Key Laboratory of Biogeology and Environmental Geology and Hubei Key Laboratory of Critical Zone Evolution, School of Earth Sciences, China University of Geosciences, Wuhan 430074, China

[5]Qinghai Provincial Key Laboratory of Geology and Environment of Salt Lakes, Qinghai Institute of Salt Lakes, Chinese Academy of Sciences, Xining 810008, China

Corresponding author: Zhixiang Wang (wangzhi8905@126.com) and Chunju Huang (huangcj@cug.edu.cn)

Key Points:

- Orbital forcing of global SSTs evolution
- Enhancement of the obliquity signal in the global SSTs at ~2.7 Ma is closely associated with the NH glaciation
- Changes in SST may drive processes of ocean-atmosphere carbon exchange that alter atmospheric CO_2 concentrations

Abstract

Changes in the thermal conditions of the ocean surface, the interface for air-sea exchange, are critical for understanding global climate and environmental change. Here we explore the evolution of sea surface temperature (SST) and the meridional sea surface temperature gradient (STG) at orbital timescales since 4 million years ago (Ma), along with interactions between SSTs, the cryosphere, and the global carbon cycle. We observe orbital eccentricity and obliquity influences on SST evolution and infer that SST changes may have played a key role in atmospheric CO_2 and cryosphere changes through key climate transitions in the past 4 Ma. We find a major equator-to-pole STG increase in the Northern Hemisphere (NH) close to the initiation of major NH glaciation (at ~2.7 Ma). In addition, we find substantial increases in the obliquity sensitivity (S_{obl}) of NH STG at ~2.7 Ma and in Southern Hemisphere (SH) STG at ~1 Ma, which may be responses to important expansions of NH and SH ice sheets, respectively. Phase analysis shows that SST changes typically lead global ice volume changes throughout the last 4 Ma. SST changes also lead atmospheric CO_2 changes since ~1.5 Ma, which indicates that SST changes either drove, or directly reflect, processes that changed ocean-atmosphere carbon exchange and, thus, atmospheric CO_2 concentrations. Overall, our study emphasizes that SST changes were a critical component of climate change throughout the last 4 Ma.

Plain Language Summary

A compilation of global sea surface temperature (SST) records indicates that SST mainly fluctuated on orbital eccentricity and obliquity timescales during the last 4 million years. The compilation also reveals an important impact of meridional ocean circulation changes on global climate since 4 Ma, with particularly notable change in the equator-to-pole SST gradient during the initiation of major Northern Hemisphere glaciations at ~2.7 Ma. Finally, we find that SST changes played a key role in the atmospheric CO_2 changes associated with global climate transformations.

1 Introduction

The oceans play a fundamental role in the climate system due to their enormous heat-storage capacity (Deser et al., 2010), and sea surface temperature (SST) changes since the early Pliocene are thought to have been a potential cause of the onset of NH glacial cycles (Fedorov et al., 2013). In addition, SST evolution profoundly affects atmospheric circulation patterns (Brierley et al., 2009; Fedorov et al., 2013), as the ocean can transfer energy to the atmosphere through turbulence and radiative energy exchange at the sea surface (Deser et al., 2010). As such, SST assessment is crucial for understanding the evolution of Earth's climate system and the mechanisms of climate change. The emergence of increasing numbers of SST records based on geochemical proxies, such as the alkenone unsaturation index ($U^{K'}_{37}$) and foraminiferal Mg/Ca ratios, has greatly improved understanding of global long-term SST evolution since the Pliocene (Liu & Herbert, 2004; Lawrence et al., 2006; Lawrence et al., 2009; O'Brien et al., 2014; Max et al., 2020). However, it remains unclear how SST affects other climate processes under changing geological boundary conditions, such as different atmospheric CO_2 concentrations (Fedorov et al., 2015).

The temperature of the ocean surface, the interface of air-sea exchange, is controlled by a combination of atmospheric and oceanic processes. The air-sea temperature contrast and wind

velocity dominate air-sea heat exchange, mainly in the form of latent and sensible heat (Cayan et al., 1992). Ocean circulation (Dowsett et al., 2009), vertical mixing (Hasenfratz et al., 2019), and thermocline depth (Wara et al., 2005) also significantly affect SST. SST records from different latitudes (Fig. 1) show large-scale variations with time similar to those in records of the oxygen isotope composition of benthic foraminifera ($\delta^{18}O_{benthic}$) and atmospheric CO_2 concentrations, but substantial differences exist at more detailed levels (Fig. 2). $\delta^{18}O_{benthic}$ is a well-established proxy for the evolution of deep-sea temperatures and seawater $\delta^{18}O$ ($\delta^{18}O_{sw}$), the latter of which is related to global ice volume (Fedorov et al., 2013; De Vleeschouwer et al., 2020; Rohling et al., 2021). Hence, similarities between large-scale variations in $\delta^{18}O_{benthic}$ and SST reflect the global nature of glacial-interglacial cycles, while differences reflect leads, lags, and amplitude response differences that may hold clues about the nature of the processes by which they are connected.

Here we focus on three issues that remain poorly explored within the past 4 million years, namely: (1) global-scale SST evolution at orbital time scales, (2) the evolution of the meridional sea surface temperature gradient (STG) between the tropics, extra-tropics, and polar regions, and (3) the relationships between SST, global ice volume, and atmospheric CO_2. We investigate the role of meridional ocean circulation changes in some of the major climate events of the last 4 Myr. The first event concerns the initiation of major NH glaciation (NHG) during the Late Pliocene-Early Pleistocene (LP/EP, ~3-2.7 Ma), when the NH transitioned from warm, virtually ice-free climatic conditions to a cold, persistent ice age climate, marked by an emerging dominance of 41-kyr obliquity cycles in $\delta^{18}O_{benthic}$ records (Lisiecki & Raymo, 2005; Westerhold et al., 2020). The second event concerns the mid-Pleistocene transition (MPT, ~1.2-0.7 Ma), when dominant 41-kyr obliquity cycles gave way to high-amplitude 100-kyr eccentricity cycles in $\delta^{18}O_{benthic}$ records (Lisiecki & Raymo, 2005; Raymo et al., 2006; Westerhold et al., 2020).

2 Materials and Methods

2.1 Data sources

The International Ocean Discovery Program (IODP) and its predecessors provided the high-quality sediment sequences used in generation of a valuable set of Cenozoic climate and sea surface temperature (SST). We use alkenone unsaturation index ($U^{K'}_{37}$) based SST records for Site 982 from the North Atlantic (58°N, 16°W; Lawrence et al., 2009), Site 607 from the North Atlantic (41°N, 33°W; Lawrence et al., 2010), Site 1012 from the North Pacific (32°N, 118°W; Brierley et al., 2009), Site 722 from the Arabian Sea (16.6°N, 59.8°W; Herbert et al., 2010), Site 846 (3°S, 91°W; Liu and Herbert, 2004; Lawrence et al., 2006), Site 1239 (1°S, 82°W; Etourneau et al., 2010) from the Equatorial Pacific, Site 662 from the Equatorial Atlantic (1°S, 12°W; Herbert et al., 2010), Site 709C from the Indian Ocean (3°54.9′S, 60°33.1′E; Karas et al., 2011), Site 1237 from the South Pacific (16°S, 76°W; Dekens et al., 2007), Site 1082 (21°S, 12°E; Etourneau et al. 2009) from the Southern Ocean, Site 1090 (43°S, 9°E; Martínez-Garcia et al. 2010) from the Subantarctic, and Site 1094 (53.2°S, 5.1°E; Hasenfratz et al., 2019) from the Antarctic Zone. The age models for the sites used in this study, with exception of Site 1237, are based on orbital tuning of deep-sea oxygen isotope records (LR04 stack; Lisiecki & Raymo, 2005; see Table S1 for details). The $U^{K'}_{37}$ index and foraminiferal Mg/Ca are widely used to reconstruct ocean temperatures. Use of the $U^{K'}_{37}$ proxy is limited in warm tropical regions, where the $U^{K'}_{37}$ index can saturate at temperatures >29°C (Li et al., 2011; Fedorov et al., 2013). We

include $U^{K'}_{37}$ based SSTs for three tropical sites (Sites 662, 846 and 1239; Supplementary Fig. S1), given that values remained below that 29°C limit (Fig. S1).

Atmospheric CO_2 concentrations are obtained from reconstructions based on leaf wax $\delta^{13}C$ at IODP Site U1446 (0-1.46 Ma; Yamamoto et al., 2022) and foraminiferal $\delta^{11}B$ (0-4 Ma; Fig. 2o; Hönisch et al., 2009; Bartoli et al., 2011; Martínez-Botí et al., 2015; Stap et al., 2016). The IODP Site U1446 leaf wax $\delta^{13}C$ record has a resolution of ~1.7 kyr, which we use for orbital-scale phase analysis. Its age model is derived from oxygen isotope tuning to the global $\delta^{18}O_{benthic}$ (LR04) stack by Clemens et al. (2021). The $\delta^{18}O_{sw}$ record in Fig. 2b has been derived from the CENOGRID $\delta^{18}O_{benthic}$ record of Westerhold et al. (2020) by Rohling et al. (2021), and has a 1 kyr resolution. The resolution of the collated datasets makes them suitable for analyzing changes in Earth's climate system at orbital time scales.

Meridional SST gradients (STG) are created by calculating the difference in SSTs between 2 ocean cores from different latitudes in the same ocean. For this study, we take these calculated STGs to be representative of the basin-wide situation as suggested by previous studies (Wara et al., 2005; Brierley et al., 2009). Due to differences between the temporal resolutions of the different SST records, we interpolated SST records from the different sites to 2 kyr spacing and then calculated the gradients. The North Atlantic STG is determined between ODP sites 982 and 662; the North Pacific STG is that between ODP Sites 846 and 1012; the South Atlantic STG uses ODP sites 1082 and 1090; and the South Pacific STG is the difference between ODP Sites 1239 and 1237.

2.2 Spectral Analysis

SST power spectra and sliding window spectrograms were calculated using Acycle 2.6 (Li et al., 2019). All records were detrended by fitting and removing LOESS functions (35%). SST power spectra were analyzed using the 2π-MultiTaper Method (MTM) with robust red noise modeling to ascertain 95% confidence levels. Eccentricity and obliquity cycles in the SST records were extracted using Gaussian band-pass filtering in Acycle 2.6 (Li et al., 2019).

2.3 Obliquity sensitivity

Obliquity sensitivity (S_{obl}) is calculated as $\sigma^2_{STG}/\sigma^2_{La04}$, where σ^2_{STG} is the temporal variance of obliquity in the STG in units of $°C^2$, and σ^2_{La04} is the temporal variance of obliquity in units of $degrees^2$, taken from the Lasker et al. (2004) orbital solution (La04). Obliquity variance was quantified using multitaper time-frequency power spectra by integrating the variance between 0.023 and 0.027 cycles/kyr (i.e., from ~43.5 kyr to 37 kyr). All time-frequency analyses were performed using three 2π prolate data tapers, with a 400-kyr window and a 10-kyr time step. The analysis was carried out in R and the R code was modified after Levy et al. (2019).

2.4 Phase analysis

SST-$\delta^{18}O_{sw}$ and SST-CO_2 phase relationships were calculated using cross-spectral analysis in the IRISSeismic package in R (Callahan et al., 2018). To visualize results, we invert $\delta^{18}O_{sw}$ to make it positively correlated with sea level. Our study focuses on phase relationships between SST, $\delta^{18}O_{sw}$, and CO_2 on eccentricity scales. We calculated cross spectra using a 400-kyr sliding window and a 10-kyr step size in individual datasets. Phase analysis calculated at the ~100-kyr eccentricity scale was chosen for a 90-135 kyr period range with the highest period coherence. The phase analysis was carried out in R and the R code was modified after De Vleeschouwer et al. (2020).

159 2.5 Recurrence analysis
160 Non-linear structure within proxy time series can help to reveal regime/system changes that
161 cannot be validated otherwise by visual inspection or linear methods like spectral analysis
162 (Marwan et al., 2007; Han et al., 2020). Recurrence analysis is used to identify transitions
163 between different types of dynamics within a time series. Recurrence plots are matrix plots that
164 visualize a fundamental property of dynamical systems – namely, when a system "repeats" itself,
165 returning to a previous state (See Text S1 for a detailed description). Recurrence plots are a
166 binary matrix where the coordinates of each entry mark the pair of time points with recurring
167 states (Marwan et al., 2007). If climate dynamics have consistent patterns, they will show up as
168 darker areas in the plot; if they have no common dynamics, the plot will remain white (Marwan
169 et al., 2007; Westerhold et al., 2020). We conducted recurrence analyses of non-detrended SST
170 data in Matlab's CRP Toolbox (Marwan, 2020).

171

172 **3 Results and Discussion**

173 **3.1 Combined high- and low-latitude forcing of regional SSTs since 4 Ma**

174 There is a strong statistical relationship between $U^{K'}_{37}$ and mean annual SST in many
175 regions (Rosell-Melé, 1998; Müller et al., 1998); hence its use as an SST proxy. However, many
176 studies have shown that coccolithophorid productivity (i.e., the main source of alkenone) is
177 highest in subpolar ocean regions during the summer to autumn months (Samtleben & Bickert,
178 1990; Lawrence et al., 2009; Max et al., 2020). A study on coccolithophore fluxes in the Bering
179 Sea and subpolar Pacific (Tsutsui et al., 2016) has further demonstrated that the main blooming
180 season and export of coccolithophores is heavily biased to October-November. Despite the
181 potential seasonal bias in the $U^{K'}_{37}$ proxy implicit in these studies, other work has suggested that
182 alkenone production may have been much less seasonal in the warm early Pliocene (Lawrence et
183 al., 2009). Overall, there is potential for the SSTs reconstructed from the $U^{K'}_{37}$ index to be
184 biased. Our analyses provide some perspective on this, as follows.
185 Our analyses highlight prominent eccentricity (both 400-kyr and 100-kyr) cycles in SST
186 records in both low and mid-latitude, and high-latitude oceans since 4 Ma (Figs. 3, 4, 5; Figs. S2,
187 S3), and this strong eccentricity cycle is also present in SST records reconstructed using
188 foraminiferal Mg/Ca (Site 709C and 1094, Figs. 4d, 5d). The eccentricity cycles in SST records
189 are consistent with theoretical eccentricity cycles (Fig. S3). Yet, annual mean insolation
190 variability at the various sites is almost entirely dominated by obliquity, and the direct impact of
191 eccentricity is very weak (Fig. S4). This agrees with obliquity cycle influences on insolation
192 (Laskar et al., 2004) and relatively negligible direct contributions of eccentricity to insolation
193 changes (<0.1%) (Clemens & Tiedemann, 1997). However, eccentricity still modulates the
194 amplitude of precession impacts, which controls the amount of summer insolation (e.g.,
195 equatorial Pacific planktonic foraminiferal Mg/Ca-based SSTs show dominant precession
196 variability since 140 ka; Jian et al., 2020). This, with additional carbon cycle changes and ice-
197 albedo effects (Pälike et al., 2006), can drive major temperature responses at low latitudes (De
198 Boer et al., 2014; Liebrand et al., 2017; Westerhold et al., 2020). Coupling between eccentricity
199 pacing and carbon cycle variations has been inferred throughout the late Neogene based on
200 carbon isotope variations (De Vleeschouwer et al., 2020), and is apparent also from orbital-scale
201 covariation between global SST and atmospheric CO_2 concentrations (Fig. 2) (also Pälike et al.,
202 2006; Liebrand et al., 2017). We infer that whatever is measured by the $U^{K'}_{37}$ index (either

annual mean SSTs, or summer and autumn SSTs) reflects predominantly precession-based summer-insolation control, where persistence of insolation-driven summer and autumn warming affects winter SSTs due to the great thermal capacity of ocean water. Our observed prominence of eccentricity variability then reflects longer-term amplitude modulation of such precession influences.

Sliding window spectrograms of SSTs in the NH and equatorial regions reveal strong obliquity (41-kyr) variability between ~2.7 Ma and ~0.7 Ma (except at Site 846; Figs. 3, 4; see also Fig. S5). Although our collection of SST records from three Southern Hemisphere sites do not show a change in the obliquity signal during the Late Pliocene, a recent Southern Hemisphere SST stack that integrates additional records reveals substantial significant obliquity enhancement around 2.7 Ma (Clark et al., 2024). Our spectral analysis of the global SST stack from the same publication shows that this enhancement of the obliquity signal at ~2.7 Ma is global in nature (Fig. S6).

Obliquity signals at high latitudes are commonly interpreted in terms of annual mean solar radiation variations (Naish et al., 2009; Bosmans et al., 2015), but the reasons for weaker obliquity before ~2.7 Ma and after ~0.7 Ma are uncertain. At low latitudes, the proportional impact of obliquity on annual mean insolation is relatively small (cf. spatio-temporal illustrations in Loutre et al., 2004; Rohling et al., 2012), but we still observe a marked obliquity signal in tropical SST records between ~2.7 and ~0.7 Ma (Fig. 4). Obliquity signals have also been found after ~2.7 Ma in other low latitude records (e.g., Lourens et al., 2001). Some studies have suggested ocean circulation as a possible mechanism for transfer of high-latitude obliquity influences to lower latitudes (Jouzel et al., 2007). Other studies have suggested that interhemispheric temperature gradients may be critical (Raymo & Nisancioglu, 2003; Li et al., 2017; Bosmans et al., 2015). Meridional temperature gradients drive both atmospheric heat and moisture transport toward the poles (Raymo & Nisancioglu, 2003; Brierley & Fedorov, 2010; Fedorov et al., 2013). However, the hemispheric insolation gradient has not changed significantly since 4 Ma, and no consensus explanation has yet been reached for the abrupt appearance of the obliquity signal at that time, for its strength across the LP/EP, or for its weakness after the MPT (especially at low latitudes) (Raymo et al., 2006; Kender et al., 2018; Yehudai et al., 2021). The explanation must include a mechanism that amplifies the Earth system response to obliquity variations, including especially its unexpected predominance at low latitudes.

To investigate this issue, we calculate meridional sea surface temperature gradients (STG) in the North Pacific, North Atlantic, South Pacific and South Atlantic (Fig. 6). We also present a new assessment of STG sensitivity to obliquity forcing (S_{obl}), which represents the ratio of obliquity-band variance in STG to the variance in obliquity (Fig. 6; see Methods). Given that previous studies have demonstrated that the influence of obliquity-driven ocean dynamics changes is amplified when Antarctic or Northern Hemisphere ice sheets expand into the marine environment (Levy et al., 2019; Cao et al., 2021), variations in S_{obl} may reflect major changes in terrestrial versus marine-based ice sheet responses to obliquity forcing (Levy et al., 2019).

We find substantial S_{obl} increases in NH STG records at ~2.7 Ma (Fig. 6b,c), without noticeable S_{obl} changes in SH STG records (Fig. 6d,e). At the same time, the STG in the NH also increased significantly at ~2.7 Ma (Fig. 6b,c). The ~2.7 Ma time interval marks the intensification of Northern Hemisphere glaciation (iNHG), which is recognized in climate proxy data that include deep-sea oxygen isotopes (Lisiecki & Raymo, 2005; Westerhold et al., 2020), North Atlantic planktonic foraminiferal assemblages (Dowsett & Poore, 1990) and ice rafted

debris records (Smith et al., 2018). This suggests that the strong global expression of obliquity in SST records at ~2.7 Ma likely resulted from S_{obl} increase associated with establishment of large-scale NH ice sheets. Conversely, a distinct S_{obl} increase in SH STG records at ~1 Ma may reflect expansion of the East Antarctica ice sheet (EAIS) margin into the ocean (Raymo et al., 2006), which would result in an enhanced response to obliquity in the SH (Levy et al., 2019). EAIS expansion into the ocean at around this time agrees with drill core data that indicate widespread expansion of a marine-based ice sheet in the Ross Embayment at the MPT (McKay et al., 2012). A S_{obl} decrease in the North Atlantic and North Pacific STGs at ~2.4 Ma (Fig. 6b, c) corresponds to a negative $\delta^{18}O_{sw}$ shift (Fig. 6a), which suggests that a reduction in global ice volume led to a S_{obl} decrease in the climate records.

3.2 Coupling between SST, carbon cycle, and cryospheric changes since 4 Ma

The causes of the iNHG at ~2.7 Ma and subsequent frequency and amplitude changes of glacial cycles remain debated (Chalk et al., 2017; Kender et al., 2018; Willeit et al., 2019; Yehudai et al., 2021). Explanations for the LP/EP and MPT climate changes often invoke atmospheric CO_2 and ice volume variations as critical links between orbital forcing and the climate response (Willeit et al., 2019; Yehudai et al., 2021). Hence, we investigate relationships between SST, global ice volume ($\delta^{18}O_{sw}$), and atmospheric CO_2 concentrations using time-evolutive SST-$\delta^{18}O_{sw}$ and SST-CO_2 phase analysis on 100-kyr eccentricity timescales (90-135 kyr period range). We use 400-kyr-wide sliding windows and 10-kyr steps to calculate leads and lags between SST, $\delta^{18}O_{sw}$, and CO_2 concentrations (see Methods). We find that SST led CO_2 concentrations for most of the time since ~1.5 Ma, with a lead of about 0-17 kyr (0-60°, Fig. 7b) (ODP Sites 662, 709C and 1237 were not used for phase analysis due to data discontinuities and their low temporal resolution). SST led global ice volume for most of the time since ~4 Ma, with a lead time of about 0-28 kyr (0-100°). However, some sites show that ice volume led SST between 2.2 and 1.5 Ma. The phase difference at these times is relatively large (50-180°; 14-50 kyr), which may suggest a decoupling between ice volume and SST between 2.2 and 1.5 Ma (Fig. 7a).

The persistent lead of SSTs over global CO_2 concentrations (since 1.5 Ma) and ice volume (since 4 Ma, except for 2.2-1.5 Ma) suggests that SST changes played an important role in global climate cycles since 4 Ma. We find that the phase difference between CO_2 and ice volume is smaller and more stable (0-25°; 0-7 kyr) than the phase difference between SST and ice volume (0-100°; 0-28 kyr), which suggests that CO_2 changes are more likely to be directly responsible for changes in global ice volume. This result could be informative also in the context of future climate change caused by anthropogenically forced increase in atmospheric CO_2. Reconstructed CO_2 data suggest a significant decrease from ~2.7 Ma (Fig. 2o), associated with the iNHG. Due to a lack of high-resolution atmospheric CO_2 reconstructions before 1.5 Ma, we have no way to determine phase relationships between CO_2, SST, and ice volume at ~2.7 Ma. However, we find that SST has continued to lead atmospheric CO_2 since ~1.5 Ma (Fig. 7b; Fig. S7). There is about 39,000 PgC of dissolved carbon storage in the oceans; more than 13 times the amount in the atmosphere and terrestrial biosphere combined (IPCC, 2007). Therefore, the mechanisms responsible for long-term changes in atmospheric CO_2 concentrations likely are ocean-related (Kohfeld and Ridgwell, 2009). Previous work has elucidated the importance of carbon redistribution between the atmosphere and ocean carbon reservoirs in driving atmospheric CO_2 changes, notably through CO_2 sequestration/release from the deep ocean (e.g., Kohfeld &

Ridgwell, 2009; Sigman et al., 2010; De Boer & Hogg, 2014; Kohfeld & Chase, 2017; Yu et al., 2014a, b, 2016, 2019, 2020; Hasenfratz et al., 2019).

Explaining the large (>100 ppm) atmospheric CO_2 drops associated with glacials requires a complex set of interconnected oceanic processes, including: 1) direct dissolution of atmospheric CO_2 into seawater (Martin et al., 2005; Kohfeld & Ridgwell, 2009; Yu et al., 2014a); 2) enhanced ocean biological pump activity (Martínez-Garcia, 2011; Hain et al., 2014); 3) weakened deep-ocean circulation (Pena & Goldstein 2014; Farmer et al. 2019); and 4) reduced CO_2 exchange between the deep sea and the surface ocean ("stratification"; Martin et al., 2005; Hasenfratz et al., 2019). Sequestered CO_2 becomes “trapped” in the deep sea, as confirmed by deep-sea [CO_3^{2-}] reconstructions (Ridgwell & Zeebe, 2005; Anderson et al., 2008; Yu et al., 2016, 2019, 2020). Air-sea disequilibrium can also enhance ocean carbon storage (Ito & Follows, 2013; Eggleston & Galbraith, 2018; Odalen et al., 2018; Khatiwala et al., 2019). In fact, previous studies in the Southern Ocean and the subarctic North Pacific based on biogenic opal accumulation and nitrogen isotope records indicate that a transition toward permanent polar ocean water-column stratification at ~2.7 Ma may have been a key driver of the atmospheric CO_2 decline (Haug et al., 1999; Sigman et al., 2010). This polar ocean stratification is thought to have been controlled by both temperature and salinity changes (Sigman et al., 2004). Our compiled dataset indicates that North Atlantic and North Pacific SSTs decreased markedly from 4 to ~2.7 Ma (ODP Sites 982 and 607; Fig. 2c, d), while the corresponding STG increased (Fig. 6b, c). NH high latitude cooling (ODP Sites 982 and 1012, Fig. 2c,e) would increase the equatorial-to-polar meridional temperature gradient (Fig. 6b,c), strengthening water vapor transport from the tropics (tropical Pacific and tropical Atlantic) to the Arctic (Loutre et al., 2004; Brierley & Fedorov, 2010) through the temperature-moisture feedback (Källén et al., 1979; Raymo & Nisancioglu, 2003). At the same time, NH high latitude cooling promotes Northern Hemisphere ice sheet development (Lunt et al., 2008; Brierley & Fedorov, 2010). High latitude cooling and increased sea ice cover cause intensification of water-column stratification (Sigman et al., 2004) and, thus, favor enhanced carbon accumulation in the deep-sea (Marinov et al., 2008; Eggleston and Galbraith, 2018; Odalen et al., 2018). In sum, oceanic processes associated with high-latitude SST reduction were crucial to atmospheric CO_2 reduction and NH glacial intensification during the Late Pliocene. This is supported by a substantial S_{obl} increase for NH STG at ~2.7 Ma (Fig. 6b,c). Several studies have proposed a simple inverse correlation between global mean surface temperature and STG measures, indicating a robust and fairly universal relationship through the past 10 million years (at low resolution) and the Eocene (on eccentricity time scales; Liu et al., 2022; Gaskell et al., 2022; Fokkema et al., 2024). Similarly, we find both a notable STG increase (Fig. 6b-d) and a distinct global sea surface temperature decrease at ~2.7 Ma (Fig. 2c-m). The predictability of this relationship between global (sea) surface temperature and STG may be relevant to future climate change.

In contrast to the atmospheric CO_2 decrease from ~2.7 Ma, there is no notable long-term (>100 kyr) atmospheric CO_2 decrease after 1 Ma (Fig. 2o), even though SST near Antarctica continued to decrease (ODP Site 1094). We note that Arctic SST (ODP Site 982) does not show this SST decrease. Inconsistent evolution of SST changes for the two poles gives a strong indication that global ice volume increases after 1 Ma had an important Antarctic component (Fig. 2b). Mid-Pleistocene high latitude cooling may have caused persistent East Antarctic ice sheet expansion into the ocean so that it no longer contained an extensive terrestrial margin, which would favor in-phase variability of NH and SH ice sheets (Raymo et al., 2006). Ocean temperature plays an important role in controlling long-term fluctuations in ice sheet margins

(Joughin et al., 2012), with marine-based ice particularly susceptible to rapid changes in ocean heat supply (Mengel & Levermann, 2014). Such mass balance sensitivity to ocean temperature has been emphasized for the EAIS (Pollard & DeConto, 2009; McKay et al., 2012; Hansen et al., 2015; Hasenfratz et al., 2019). Overall, therefore, we infer that EAIS variability may have become amplified from ~1 Ma by the development of an extensive marine ice sheet margin.

To test our argument about fundamental transitions in the relationships between SST, STG, and high-latitude ice sheets, we performed recurrence analyses of the NH and SH STG, as well as global ice volume ($\delta^{18}O_{sw}$). Results highlight major global ice volume shifts at ~2.7 Ma and ~1 Ma (Fig. 8a), consistent with previous studies that suggest a major global climate transition associated with high-latitude ice sheet development (Westerhold et al., 2020). Recurrence analyses of STG in the North Atlantic and North Pacific (ODP Sites 662-982 and 846-1012; Fig. 8b,c) show a major shift at ~2.7 Ma, suggesting a link between NH STG and iNHG. Conversely, recurrence analyses of STG in the South Atlantic and South Pacific (Sites 1082-1090 and 1239-1237; Fig. 8d,e) show a major transition at ~1 Ma, in agreement with the aforementioned concept of widespread marine AIS margin development. The recurrence analyses, therefore, support our previous interpretations that there were two key climate transitions since 4 Ma (LP/EP and MPT) that contained critical involvement of SST and STG changes with distinctly different expressions (and, hence, governing processes) between the two hemispheres.

4 Conclusions

We compiled globally distributed SST records to investigate the involvement of orbital-scale SST trends and oceanic meridional temperature gradient changes in key climate transitions during the last 4 million years. We observe important orbital eccentricity and obliquity influences in the SST evolution, and infer both summer insolation and high-latitude ice volume (feedback) impacts on global SST. We find that the SST in the NH and the equatorial region shows a significant enhancement of the obliquity signal at ~2.7 Ma, and at the same time, the NH meridional SST gradient as well as its obliquity sensitivity also increases sharply at ~2.7 Ma. We infer that the enhancement of the obliquity signal in the NH and equatorial region during this period originates from large-scale NH ice sheet expansion. In addition, the increase in obliquity sensitivity of the southern hemisphere meridional SST gradient at ~1 Ma may be attributed to oceanward expansion of the Antarctic ice sheet margin. Phase analysis revealed key links between variations in SST, global ice volume, and atmospheric CO_2 levels, which underpinned the major climate shifts. Changes in SST can directly affect not only the formation and development of high-latitude ice sheets, but also global temperatures and thus ice volume by controlling changes in the atmospheric CO_2 concentration.

Acknowledgments

This work was supported by the National Natural Science Foundation of China (Grant No. 42230208; 42172039; 42272033) and Postdoctoral Fellowship Program of CPSF (GZC20232471). EJR was supported by the Australian Centre for Excellence in Antarctic Science, an Australian Research Council Special Research Initiative (Project Number SR200100008).

Open Research

The sea surface temperature data are available at Zhang (2024a). The data analysis was carried out in R. The complete codes reported in this study are available at Zhang (2024b).

References

Anderson, R. F., *et al.* Modern $CaCO_3$ preservation in equatorial Pacific sediments in the context of late-Pleistocene glacial cycles. *Marine Chemistry* **111**, 30-46 (2008).

Bartoli, G., Hönisch, B., Zeebe, R. E. Atmospheric CO_2 decline during the Pliocene intensification of Northern Hemisphere glaciations. *Paleoceanography* **26** (2011).

Bosmans, J. H. C., *et al*. Obliquity forcing of low-latitude climate. *Clim. Past* **11**, 1335-1346 (2015).

Brierley, C. M. *et al*. Greatly expanded tropical warm pool and weakened Hadley circulation in the early Pliocene. *Science* **323**, 1714-1718 (2009).

Brierley, C. M., Fedorov, A. V. Relative importance of meridional and zonal sea surface temperature gradients for the onset of the ice ages and Pliocene-Pleistocene climate evolution. *Paleoceanography* **25** (2010).

Callahan, J., *et al*. IRISSeismic: Classes and Methods for Seismic Data Analysis https://cran.r-project.org/web/ packages/IRISSeismic/index.html (2018).

Cao, M. M. *et al*. Mineral Dust Coupled With Climate-Carbon Cycle on Orbital Timescales Over the Past 4 Ma. *Geophys. Res. Lett.* **48**, e2021GL095327 (2021).

Cayan, D. R. Latent and sensible heat flux anomalies over the northern oceans: driving the sea surface temperature. *J. Phys. Oceanogr*. **22**, 859-881 (1992).

Chalk, T. B. *et al*. Causes of ice age intensification across the Mid-Pleistocene Transition. *Proc. Natl. Acad. Sci. U.S.A.* **114**, 13114-13119 (2017).

Clark, P. U., *et al*. Global and regional temperature change over the past 4.5 million years. *Science* **383**, 884-890 (2024).

Clemens, S. C., Tiedemann, R. Eccentricity forcing of Pliocene-early Pleistocene climate revealed in a marine oxygen-isotope record. *Nature* **385**, 801-804 (1997).

De Boer, A. M., Hogg, A. M. Control of the glacial carbon budget by topographically induced mixing. *Geophys. Res. Lett.* **41**, 4277-4284 (2014).

De Boer, B., Lourens, L. J., van de Wal, R. S. W. Persistent 400,000-year variability of Antarctic ice volume and the carbon cycle is revealed throughout the Plio-Pleistocene. *Nat. Commun.* **5**, 1-8 (2014).

De Vleeschouwer, D. *et al*. High-latitude biomes and rock weathering mediate climate-carbon cycle feedbacks on eccentricity timescales. *Nat. Commun.* **11**, 5013 (2020).

Dekens, P. S., *et al*. Core top calibration of Mg/Ca in tropical foraminifera: Refining paleotemperature estimation. *Geochem. Geophy. Geosy*. **3**, 1-29 (2002).

Dekens, P. S., Ravelo, A. C., McCarthy, M. D. Warm upwelling regions in the Pliocene warm period. *Paleoceanography* **22** (2007).

Deser, C., *et al*. Sea surface temperature variability: Patterns and mechanisms. *Annu. Rev. Mar. Sci.* **2**, 115-143 (2010).

Dowsett, H. J., Poore, R. Z. A new planktic foraminifer transfer function for estimating Pliocene through Holocene sea surface temperatures. *Mar. Micropaleontol.* **16**, 1-23 (1990).

Dowsett, H. J., Robinson, M. M., Foley, K. M. Pliocene three-dimensional global ocean temperature reconstruction. *Clim. Past* **5**, 769-783 (2009).

Eggleston, S., Galbraith, E. D. The devil's in the disequilibrium: multi-component analysis of dissolved carbon and oxygen changes under a broad range of forcings in a general circulation model. *Biogeosciences* **15**, 3761-3777 (2018).

Eroglu, D. *et al*. See-saw relationship of the Holocene East Asian-Australian summer monsoon. *Nat. Commun.* **7**, 12929 (2016).

Etourneau, J., *et al*. Pliocene-Pleistocene variability of upwelling activity, productivity, and nutrient cycling in the Benguela region. *Geology* **37**, 871-874 (2009).

Etourneau, J., *et al*. Intensification of the Walker and Hadley atmospheric circulations during the Pliocene-Pleistocene climate transition. *Earth Planet. Sci. Lett.* **297**, 103-110 (2010).

Farmer, J. R. *et al*. Deep Atlantic Ocean carbon storage and the rise of 100,000-year glacial cycles. *Nat. Geosci.* **12**, 355-360 (2019).

Fedorov, A. V. *et al*. Patterns and mechanisms of early Pliocene warmth. *Nature* **496**, 43-49 (2013).

Fedorov, A. V., *et al*. Tightly linked zonal and meridional sea surface temperature gradients over the past five million years. *Nat. Geosci.* **8**, 975-980 (2015).

Fokkema, C. D., *et al*. Polar amplification of orbital-scale climate variability in the early Eocene greenhouse world. *Clim. Past* **20**, 1303-1325 (2024).

Gaskell, D. E., *et al*. The latitudinal temperature gradient and its climate dependence as inferred from foraminiferal $\delta^{18}O$ over the past 95 million years. *Proc. Natl. Acad. Sci. U. S. A.* **119**, e2111332119 (2022).

Hain, M. P., Sigman, D. M., Haug, G. H. The biological Pump in the Past. Reference Module in Earth Systems and Environmental Sciences, treatise on Geochemistry (Second Edition). *The Oceans and Marine Geochemistry* **8**, 485-517 (2014).

Han, W. X., *et al*. Climate transition in the Asia inland at 0.8-0.6 Ma related to astronomically forced ice sheet expansion. *Quat. Sci. Rev.* **248**, 106580 (2020).

Hasenfratz, A. P. *et al.* The residence time of Southern Ocean surface waters and the 100,000-year ice age cycle. *Science* **363**, 1080-1084 (2019).

Haug, G. H., *et al*. Onset of permanent stratification in the subarctic Pacific Ocean. *Nature* **401**, 779-782 (1999).

Herbert, T. D., *et al*. Tropical ocean temperatures over the past 3.5 million years. *Science* **328**, 1530-1534 (2010).

Hönisch, B., *et al*. Atmospheric carbon dioxide concentration across the Mid-Pleistocene transition. *Science* **324**, 1551-1554 (2009).

IPCC. Climate Change 2007: The Physical Science Basis. Contribution of Working Group I to the Fourth Assessment Report of the Intergovernmental Panel on Climate Change, 996 pp., Cambridge Univ. Press, Cambridge, U. K. (2007).

Ito, T., Follows, M. J. Air-sea disequilibrium of carbon dioxide enhances the biological carbon sequestration in the Southern Ocean. *Global Biogeochem. Cy.* **27**, 1129-1138 (2013).

Jian, Z., *et al*. Half-precessional cycle of thermocline temperature in the western equatorial Pacific and its bihemispheric dynamics. *Proc. Natl. Acad. Sci. U. S. A.* **117**, 7044-7051 (2020).

Joughin, I., Alley, R. B., Holland, D. M. Ice-sheet response to oceanic forcing. *Science* **338**, 1172-1176 (2012).

Jouzel, J., *et al.* Orbital and millennial Antarctic climate variability over the past 800,000 years. *Science* **317**, 793-796 (2007).

Källén, E., Crafoord, C., Ghil, M. Free oscillations in a climate model with ice-sheet dynamics. *J. Atmos. Sci.* **36**, 2292-2303 (1979).

Karas, C., *et al*. Pliocene Indonesian Throughflow and Leeuwin Current dynamics: implications for Indian Ocean polar heat flux. *Paleoceanography* **26**, PA2217 (2011).

Kender, S., *et al*. Closure of the Bering Strait caused mid-Pleistocene transition cooling. *Nat. Commun.* **9**, 1-11 (2018).

Khatiwala, S., Schmittner, A., Muglia, J. Air-sea disequilibrium enhances ocean carbon storage during glacial periods. *Sci. Adv.* **5**, eaaw4981 (2019).

Kohfeld, K. E., Chase, Z. Temporal evolution of mechanisms controlling ocean carbon uptake during the last glacial cycle. *Earth Planet. Sci. Lett.* **472**, 206-215 (2017).

Kohfeld, K. E., Ridgwell, A. Glacial-interglacial variability in atmospheric CO_2. *Surface ocean-lower atmosphere processes* **187**, 251-286 (2009).

Laskar, J. *et al*. A long-term numerical solution for the insolation quantities of the Earth. *Astron. Astrophys*. **428**, 261-285 (2004).

Lawrence, K. T., Liu, Z., Herbert, T. D. Evolution of the eastern tropical Pacific through Plio-Pleistocene glaciation. *Science* **312**, 79-83 (2006).

Lawrence, K. T., *et al*. North Atlantic climate evolution through the Plio-Pleistocene climate transitions. *Earth Planet. Sci. Lett.* **300**, 329-342 (2010).

Lawrence, K., *et al*. High-amplitude variations in North Atlantic sea surface temperature during the early Pliocene warm period. *Paleoceanography* **24**, PA2218 (2009).

Levy, R. H. *et al*. Antarctic ice-sheet sensitivity to obliquity forcing enhanced through ocean connections. *Nat. Geosci.* **12**, 132-137 (2019).

Li, L. *et al*. A 4-Ma record of thermal evolution in the tropical western Pacific and its implications on climate change. *Earth Planet. Sci. Lett.* **309**, 10-20 (2011).

Li, M. S., Hinnov, L., Kump, L. Acycle: time-series analysis software for paleoclimate research and education. *Comput. Geosci.* **127**, 12-22 (2019).

Li, T., *et al.* Continued obliquity pacing of East Asian summer precipitation after the mid-Pleistocene transition. *Earth Planet. Sci. Lett.* **457**, 181-190 (2017).

Liebrand, D. *et al*. Evolution of the early Antarctic ice ages. *Proc. Natl. Acad. Sci. U.S.A.* **114**, 3867-3872 (2017).

Lisiecki, L. E., Raymo, M. E. A Pliocene-Pleistocene stack of 57 globally distributed benthic $\delta^{18}O$ records. *Paleoceanography* **20**, 1003 (2005).

Liu, Z. H., Herbert, T. D. High-latitude influence on the eastern equatorial Pacific climate in the early Pleistocene epoch. *Nature* **427**, 720-723 (2004).

Liu, X., *et al*. Persistent high latitude amplification of the Pacific Ocean over the past 10 million years. *Nat. Commun*. **13**, 7310 (2022).

Lourens, L. J., Wehausen, R., Brumsack, H. J. Geological constraints on tidal dissipation and dynamical ellipticity of the Earth over the past three million years. *Nature* **409**, 1029-1033 (2001).

Loutre, M. F., *et al*. Does mean annual insolation have the potential to change the climate? *Earth Planet. Sci. Lett.* **221**, 1-14 (2004).

Lunt, D. J., *et al*. Late Pliocene Greenland glaciation controlled by a decline in atmospheric CO_2 levels. *Nature* **454**, 1102-1105 (2008).

Lüthi, D., *et al*. CO_2 and O_2/N_2 variations in and just below the bubble–clathrate transformation zone of Antarctic ice cores. *Earth Planet. Sci. Lett*. **297**, 226-233 (2010).

Mann, M. E., Lees, J. M. Robust estimation of background noise and signal detection in climatic time series. *Clim. Change* **33**, 409-445 (1996).

Marinov, I., *et al*. Impact of oceanic circulation on biological carbon storage in the ocean and atmospheric pCO_2. *Global Biogeochemical Cycles* **22** (2008).

Martin, P., Archer, D., Lea, D. W. Role of deep sea temperature in the carbon cycle during the last glacial. *Paleoceanography* **20** (2005).

Martínez-Botí, M., *et al*. Plio-Pleistocene climate sensitivity evaluated us-ing high-resolution CO_2 records. *Nature* **518**, 49-54 (2015).

Martínez-Garcia, A., *et al*. Southern Ocean dust-climate coupling over the past four million years. *Nature* **476**, 312-315 (2011).

Martínez-Garcia, A., *et al*. Subpolar link to the emergence of the modern equatorial Pacific cold tongue. *Science* **328**, 1550-1553 (2010).

Marwan, N. Cross Recurrence Plot Toolbox for MATLAB®, Ver. 5.22 (R32.4), http://tocsy.pik-potsdam.de/CRPtoolbox/accessed 2020-12-09 (2020).

Marwan, N., *et al*. Recurrence Plots for the Analysis of Complex Systems. *Phys. Rep.* **438**, 237-329 (2007).

Max, L., *et al*. Evaluation of reconstructed sea surface temperatures based on $U^{K'}_{37}$ from sediment surface samples of the North Pacific. *Quaternary Sci. Rev.* **243**, 106496 (2020).

McKay, R. *et al*. Pleistocene variability of Antarctic ice sheet extent in the Ross embayment. *Quaternary Sci. Rev.* **34**, 93-112 (2012).

Mengel, M., Levermann, A. Ice plug prevents irreversible discharge from East Antarctica. *Nat. Clim. Change* **4**, 451-455 (2014).

Monnin, E., *et al*. Atmospheric CO_2 concentrations over the last glacial termination. *Science* **291**, 112-114 (2001).

Müller, P. J., *et al*. Calibration of the alkenone paleotemperature index $U_{37}^{K'}$ based on core-tops from the eastern South Atlantic and the global ocean (60°N - 60 °S). *Geochem. Cosmochim. Acta* **62**, 1757-1772 (1998).

Naish, T. *et al*. Obliquity-paced Pliocene West Antarctic ice sheet oscillations. *Nature* **458**, 322-328 (2009).

O'Brien, C. L. *et al.* High sea surface temperatures in tropical warm pools during the Pliocene. *Nat. Geosci.* **7**, 606-611 (2014).

Odalen, M., *et al*. The influence of the ocean circulation state on ocean carbon storage and CO_2 drawdown potential in an Earth system model. *Biogeosciences* **15**, 1367-1393 (2018).

Pälike, H., *et al*. The heartbeat of the Oligocene climate system. *Science* **314**, 1894-1898 (2006).

Pena, L. D., Goldstein, S. L. Thermohaline circulation crisis and impacts during the mid-Pleistocene transition. *Science* **345**, 318-322 (2014).

Pépin, L., *et al*. Hemispheric roles of climate forcings during glacial-interglacial transitions as deduced from the Vostok record and LLN-2D model experiments. *Journal of Geophysical Research: Atmospheres* **106**, 31885-31892 (2001).

Petit, J. R., *et al*. Climate and atmospheric history of the past 420,000 years from the Vostok ice core, Antarctica. *Nature* **399**, 429-436 (1999).

Pollard, D., DeConto, R. M. Modelling West Antarctic ice sheet growth and collapse through the past five million years. *Nature* **458**, 329-332 (2009).

Raymo, M. E., Lisiecki, L. E., Nisancioglu, K. H. Plio-Pleistocene ice volume, Antarctic climate, and the global $\delta^{18}O$ record. *Science* **313**, 492-495 (2006).

Raymo, M. E., Nisancioglu, K. H. The 41 kyr world: Milankovitch's other unsolved mystery. *Paleoceanography* **18** (2003).

Raynaud, D., *et al*. The record for marine isotopic stage 11. *Nature* **436**, 39-40 (2005).

Ridgwell, A., Zeebe, R. E. The role of the global carbonate cycle in the regulation and evolution of the Earth system, *Earth Planet. Sci. Lett.* **234**, 299-315 (2005).

Rohling, E. J., *et al.* Sea level and deep-sea temperature reconstructions suggest quasi-stable states and critical transitions over the past 40 million years. *Sci. Adv.* **7**, eabf5326 (2021).

Rohling, E. J., *et al*. Sea surface and high-latitude temperature sensitivity to radiative forcing of climate over several glacial cycles. *J. Climate* **25**, 1635-1656 (2012).

Rosell-Melé, A. Interhemispheric appraisal of the value of alkenone indices as temperature and salinity proxies in high-latitude locations. *Paleoceanography* **13**, 694-703 (1998).

Samtleben, C., Bickert, T. Coccoliths in sediment traps from the Norwegian Sea. *Mar. Micropaleontol.* **16**, 39-64 (1990).

Schinkel, S., Dimigen, O., Marwan, N. Selection of recurrence threshold for signal detection. *European Physical Journal Special Topics* **164**, 45-53 (2008).

Siegenthaler, U. R. S., *et al*. Supporting evidence from the EPICA Dronning Maud Land ice core for atmospheric CO_2 changes during the past millennium. *Tellus B: Chemical and Physical Meteorology* **57**, 51-57 (2005a).

Siegenthaler, U., *et al*. Stable carbon cycle–climate relationship during the Late Pleistocene. *Science* **310**, 1313-1317 (2005b).

Sigman, D. M., Hain, M. P., Haug, G. H. The polar ocean and glacial cycles in atmospheric CO_2 concentration. *Nature* **466**, 47-55 (2010).

Sigman, D. M., Jaccard, S., Haug, G. H. Polar ocean stratification in a cold climate. *Nature* **428**, 59-63 (2004).

Smith, Y. M. *et al*. Icebergs in the Nordic Seas Throughout the Late Pliocene. *Paleoceanogr. Paleoclimatol.* **33**, 318-335 (2018).

Stap, L. B. *et al*. CO_2 over the past 5 million years: Continuous simulation and new $\delta^{11}B$-based proxy data. *Earth Planet. Sci. Lett.* **439**, 1-10 (2016).

Tsutsui, H., *et al*. Nineteen-year time-series sediment trap study of Coccolithus pelagicus and Emiliania huxleyi (calcareous nannoplankton) fluxes in the Bering Sea and subarctic Pacific Ocean. *Deep-Sea Res. Part II Top. Stud. Oceanogr.* **125**, 227-239 (2016).

Vázquez Riveiros, N., *et al*. Mg/Ca thermometry in planktic foraminifera: Improving paleotemperature estimations for G. bulloides and N. pachyderma left. *Geochem. Geophy. Geosy*. **17**, 1249-1264 (2016).

Westerhold, T., *et al*. An astronomically dated record of Earth's climate and its predictability over the last 66 million years. *Science* **369**, 1383-1387 (2020).

Willeit, M., *et al*. Mid-Pleistocene transition in glacial cycles explained by declining CO_2 and regolith removal. *Sci. Adv.* **5**, eaav7337 (2019).

Yamamoto, M., *et al*. Increased interglacial atmospheric CO_2 levels followed the mid-Pleistocene Transition. *Nat. Geosci.* **15**, 307-313 (2022).

Yehudai, M., *et al.* Evidence for a Northern Hemispheric trigger of the 100,000-y glacial cyclicity. *Proc. Natl. Acad. Sci. U.S.A.* **118** (2021).

Yu, J., *et al*. Deep South Atlantic carbonate chemistry and increased interocean deep water exchange during last deglaciation. *Quaternary Sci. Rev.* **90**, 80-89 (2014b).

Yu, J., *et al*. Last glacial atmospheric CO_2 decline due to widespread Pacific deep water expansion. *Nat. Geosci.* **13**, 628-633 (2020).

Yu, J., *et al*. More efficient North Atlantic carbon pump during the Last Glacial Maximum. *Nat. Commun.* **10**, 2170 (2019).
Yu, J., *et al*. Sequestration of carbon in the deep Atlantic during the last glaciation. *Nat. Geosci.* **9**, 319-324 (2016).
Yu, J., Anderson, R. F., Rohling, E. J. Deep ocean carbonate chemistry and glacial-interglacial atmospheric CO_2 changes. *Oceanography* **27**, 16-25 (2014a).
Zhang, Z. Sea surface temperature data reconstructed by unsaturated alkenone index and foraminiferal Mg/Ca since 4 Ma. Version 2 [Dataset]. 4TU. ResearchData (2024a). https://doi.org/10.4121/20486157.
Zhang, Z. R code for Obliquity sensitivity and phase analysis. Version 1 [Software]. 4TU. ResearchData (2024b). https://doi.org/10.4121/2904d0f4-0f50-45f4-8363-69574ac1b2e5.

Figure 1. Map of sites (black dots) from which data were retrieved (data are from: Lawrence et al., 2006, 2009, 2010; Brierley et al. 2009; Etourneau et al. 2009, 2010; Dekens et al. 2007; Herbert et al., 2010; Liu & Herbert, 2004; Karas et al., 2011; Martínez-Garcia et al. 2010; Hasenfratz et al., 2019), superimposed on a map of modern annual mean SST (contours and colours after Fedorov et al., 2013). Numbers indicate sites from the Deep Sea Drilling Project (DSDP), the Ocean Drilling Program (ODP), the Integrated Ocean Drilling Program and International Ocean Discovery Program (both IODP), and the International Marine Global Change Study (IMAGES). Black arrows indicate modern global ocean circulation. Acronyms: Atlantic Drift (NAD), Gulf Stream (GS), North Equatorial Current (NEC), South Equatorial Current (SEC), Humboldt Current (HC), Labrador Current (LC), California Current (CC), Equatorial Counter Current (ECC), Thousand Islands Cold Current (TICC), Kuroshio (Kuro.), Canary Cold Stream (CCS), Benguela Current (BC), Somali Warm Current (SWC), and Western Australian Cold Stream (WACS).

Figure 2. SST and CO_2 concentration records shown with benthic foraminiferal $\delta^{18}O$ and seawater $\delta^{18}O_{sw}$ for the past 4000 kyr (4 Myr). a) Benthic foraminiferal $\delta^{18}O$ (LR04 stack;

Lisiecki & Raymo, 2005). b) Seawater $\delta^{18}O_{sw}$ (proxy for global ice volume; Rohling et al., 2021). The direction of the arrow indicates increasing ice volume. c) Sea surface temperature of ODP Sites 982 (North Atlantic; Lawrence et al., 2009). d) Sea surface temperature of DSDP Site 607 (North Atlantic; Lawrence et al., 2010). e) Sea surface temperature of ODP Site 1012 (North Pacific; Brierley et al., 2009). f) Sea surface temperature of ODP Site 722 (Arabian Sea; Herbert et al., 2010). g) Sea surface temperature of ODP Site 1239 (Eastern equatorial Pacific; Etourneau et al., 2010). h) Sea surface temperature of ODP Site 662 (Equatorial Atlantic; Herbert et al., 2010). i) Sea surface temperature of ODP Site 846 (Eastern equatorial Pacific; Liu & Herbert, 2004; Lawrence et al., 2006). j) Sea surface temperature of ODP Site 709C (Indian Ocean; Karas et al., 2011). k) Sea surface temperature of ODP Site 1237 (South Pacific; Dekens et al., 2007). l) Sea surface temperature of ODP Site 1082 (South Atlantic; Etourneau et al., 2009). m) Sea surface temperature of ODP Site 1090 (Subantarctic; Martínez-Garcia et al., 2010). n) Sea surface temperature of ODP Site 1094 (Antarctic; Hasenfratz et al., 2019). o) Estimated atmospheric CO_2 concentrations (Yamamoto et al., 2022; Stap et al., 2016; Martínez-Botí et al., 2015; Bartoli et al., 2011; Hönisch et al., 2009).

Figure 3. Astronomical evolution of SSTs from ocean drilling sites at different latitudes in the Northern Hemisphere. Spectrograms with 600 kyr sliding windows with 2π multi-taper (MTM) power spectra of (a) SST of ODP Site 982 since 4 Ma, (b) SST of DSDP Site 607 since 4 Ma, (c) SST of ODP Site 1012 since 4 Ma, (d) SST of ODP Site 722 since ~3.3 Ma. SSTs from these sites were reconstructed using $U^{K'}_{37}$. The red dotted line on the left side of the spectrograms are the 95% confidence levels. The ticks on the power x-axes indicate the strength of the periodic signal in the spectrogram. The colors in the sliding window spectrogram indicate

659 the strength of the periodic signal, with blue-grayish blue-green indicating an increasingly strong
660 periodic signal. The white shaded band indicates the enhancement of the obliquity signal at ~2.7
661 Ma.
662
663 **Figure 4. Astronomical evolution of SST from ocean drilling sites in the equatorial region.**
664 Spectrograms with 600 kyr sliding windows with 2π multi-taper (MTM) power spectra of (a)
665 SST of ODP Site 662 since 4 Ma, (b) SST of ODP Site 1239 since 4 Ma, (c) SST of ODP Site
666 846 since ~3.9 Ma, (d) SST of ODP Site 709C from ~4.9 to ~2.2 Ma. SST of ODP Sites 709C
667 were reconstructed using foraminiferal Mg/Ca, and the remaining SST temperatures were
668 reconstructed using $U^{K'}_{37}$. The red dotted line on the left side of the spectrograms are the 95%
669 confidence levels. The ticks on the power x-axes indicate the strength of the periodic signal in
670 the spectrogram. The colors in the sliding window spectrogram indicate the strength of the
671 periodic signal, with blue-grayish blue-green indicating an increasingly strong periodic signal.
672 The white shaded band indicates the enhancement of the obliquity signal at ~2.7 Ma.
673
674 **Figure 5. Astronomical evolution of SST from ocean drilling sites at different latitudes in**
675 **the Southern Hemisphere.** Spectrograms with 600 kyr sliding windows with 2π multi-taper
676 (MTM) power spectra of (a) SST of ODP Site 1237 since 4 Ma, (b) SST of ODP Site 1082 since
677 ~3.5 Ma, (c) SST of ODP Site 1090 since ~3.6 Ma, (d) SST of ODP Site 1094 from 1.5 to 0.9
678 Ma. ODP Sites 1094 were reconstructed using foraminiferal Mg/Ca, and the remaining SST
679 temperatures were reconstructed using $U^{K'}_{37}$. Note that the absence of an obliquity signal in the
680 SST record at ODP Site 1237 is likely due to this record's lower temporal resolution (~14 kyr).
681 The red dotted line on the left side of the spectrograms are the 95% confidence levels. The ticks

on the power x-axes indicate the strength of the periodic signal in the spectrogram. The colors in the sliding window spectrogram indicate the strength of the periodic signal, with blue-grayish blue-green indicating an increasingly strong periodic signal.

Figure 6. Meridional SST gradients (STG) and STG obliquity sensitivity (S_{obl}) for the North Atlantic, North Pacific, South Atlantic and South Pacific since 4 Ma. a) Seawater $\delta^{18}O_{sw}$ (proxy for global ice volume; Rohling et al., 2021). The black arrow indicates increasing ice volume. b) Meridional SST gradients between ODP Sites 846 (3°S, 91°W; Liu & Herbert, 2004; Lawrence et al., 2006) and 1012 (32°N, 118°W; Brierley et al. 2009) for North Pacific and obliquity sensitivity (S_{obl}). c) Meridional SST gradients between ODP Site 662 (1°S, 12°W; Herbert et al., 2010) and 982 (58°N, 16°W; Lawrence et al., 2009) for North Atlantic and obliquity sensitivity (S_{obl}). d) Meridional SST gradients between ODP Sites 1239 (1°S, 82°W; Etourneau et al. 2010) and 1237 (16°S, 76°W; Dekens et al. 2007) for South Pacific and obliquity sensitivity (S_{obl}). e) Meridional SST gradients between ODP Sites 1082 (21°S, 12°E; Etourneau et al. 2009) and 1090 (43°S, 9°E; Martínez-Garcia et al. 2010) for South Atlantic and obliquity sensitivity (S_{obl}). The thick black lines are $S_{obl.}$

Figure 7. Phase analysis of SST-$\delta^{18}O_{sw}$ and SST-CO_2 concentrations at the 100-kyr eccentricity scale over the past 4 Ma. A typical confidence interval is ±6°. The $\delta^{18}O_{sw}$ data are from Rohling et al. (2021), atmospheric CO_2 concentrations are obtained from reconstruction based on leaf wax $\delta^{13}C$ at IODP Site U1446 (0-1.46 Ma; Yamamoto et al., 2022). Note that the red symbols and lines indicate SSTs in the NH, the green symbols and lines indicate SSTs in the

equatorial regions, and the blue symbols and lines indicate SSTs in the SH. The time is based on the centre of the window.

Figure 8. Recurrence plots of Global ice volume ($\delta^{18}O_{sw}$) and STG in the NH and SH. a-e show recurrence plots of $\delta^{18}O_{sw}$ (global ice volume), STG in the North Atlantic, STG in the North Pacific, STG in the South Atlantic and STG in the South Pacific, respectively. The red arrows on top of the recurrence plots indicate points in time when transitions occurred. Transitions in these recurrence plots from darker areas to white areas indicate prominent systems changes (Marwan et al., 2007), see also Section 2.5 for further details. Global ice volume shows changes at ~2.7 and ~1 Ma. NH STG (ODP 662-982; ODP 846-1012) show a change at ~2.7 Ma; SH STG (ODP 1239-1237; ODP 1082-1090) show a change at ~1 Ma. Note that subplot b has a different time axis than all the other subplots due to the lack of SST data between ~1.5-0.5 Ma of ODP 662 in the North Atlantic.

Figure 1.

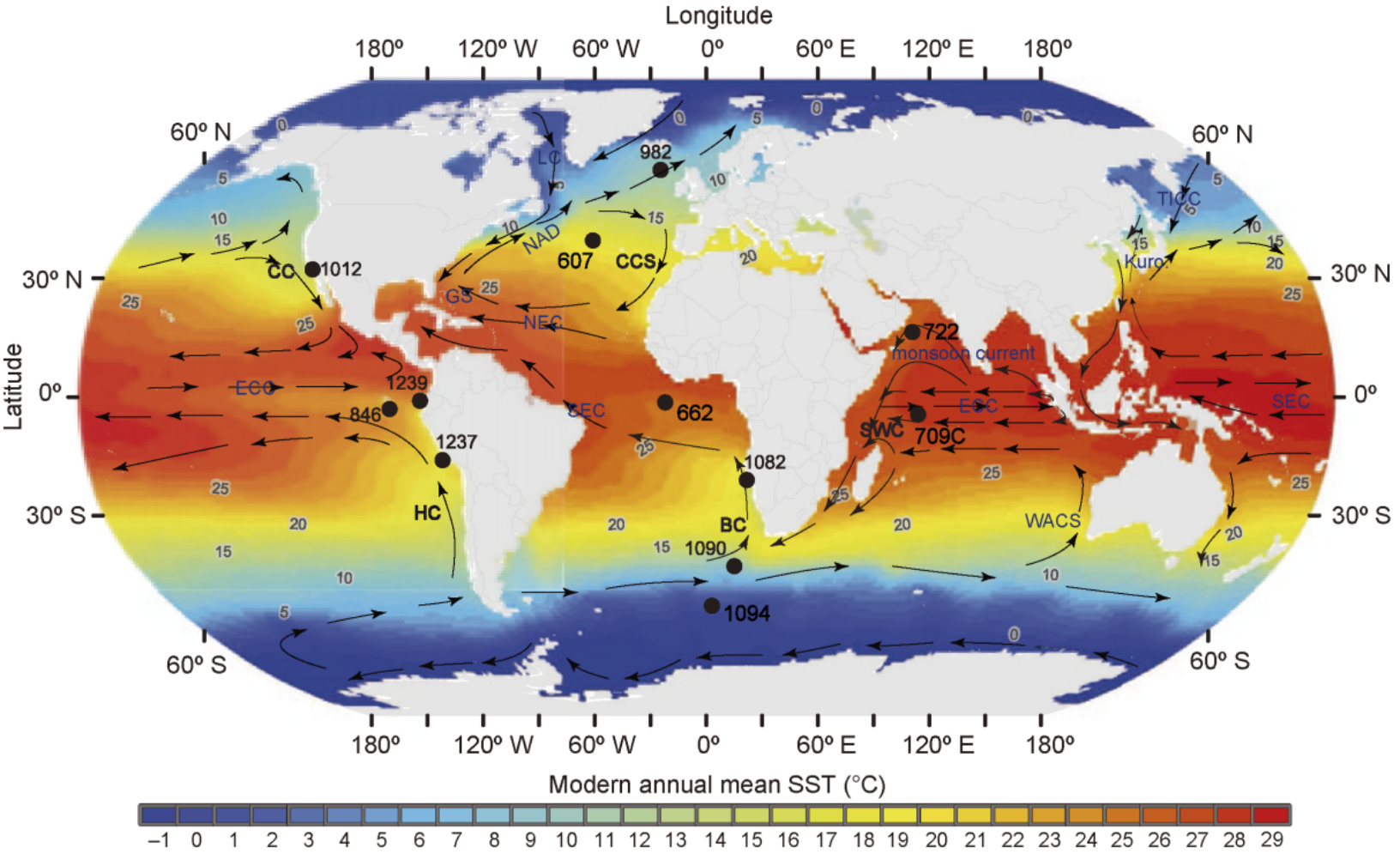
Longitude
180°
120° W
60° W
0°
60° E
120° E
180°
60° N
30° N
0°
30° S
60° S
Latitude
LC
982
NAD
607
CCS
CC
1012
GS
NEC
722
monsoon current
ECC
1239
846
CEC
662
SWC
709C
1237
1082
HC
BC
1090
1094
WACS
TICC
Kuro
SEC
Modern annual mean SST (°C)
–1 0 1 2 3 4 5 6 7 8 9 10 11 12 13 14 15 16 17 18 19 20 21 22 23 24 25 26 27 28 29

Figure 2.

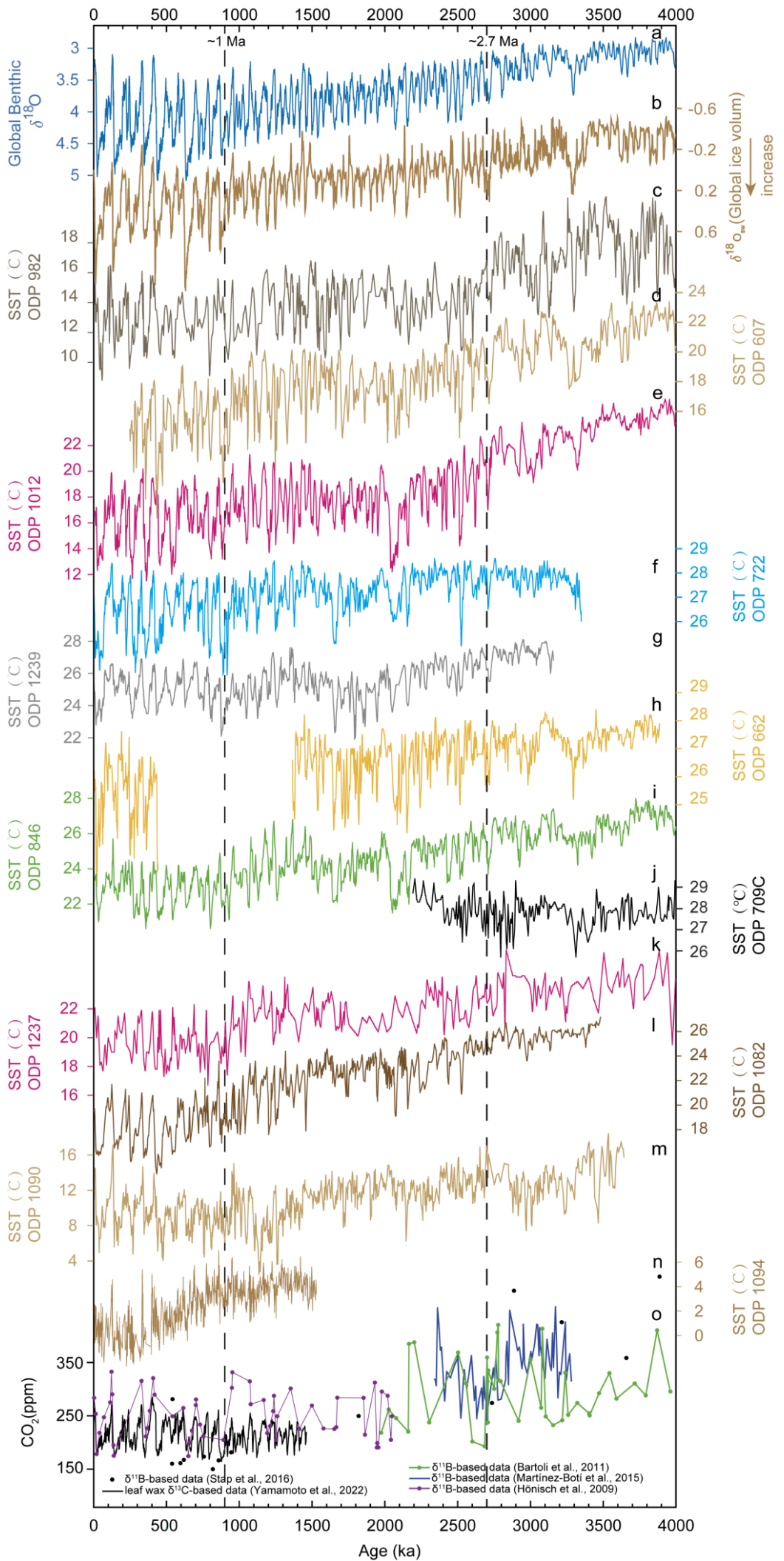
~1 Ma
~2.7 Ma
a
b
c
d
e
f
g
h
i
j
k
l
m
n
o
Global Benthic δ18O
δ18Osw (Global ice volum) increase
SST (°C) ODP 982
SST (°C) ODP 607
SST (°C) ODP 1012
SST (°C) ODP 722
SST (°C) ODP 1239
SST (°C) ODP 662
SST (°C) ODP 846
SST (°C) ODP 709C
SST (°C) ODP 1237
SST (°C) ODP 1082
SST (°C) ODP 1090
SST (°C) ODP 1094
CO2 (ppm)
δ11B-based data (Stap et al., 2016)
leaf wax δ13C-based data (Yamamoto et al., 2022)
δ11B-based data (Bartoli et al., 2011)
δ11B-based data (Martínez-Botí et al., 2015)
δ11B-based data (Hönisch et al., 2009)
Age (ka)

Figure 3.

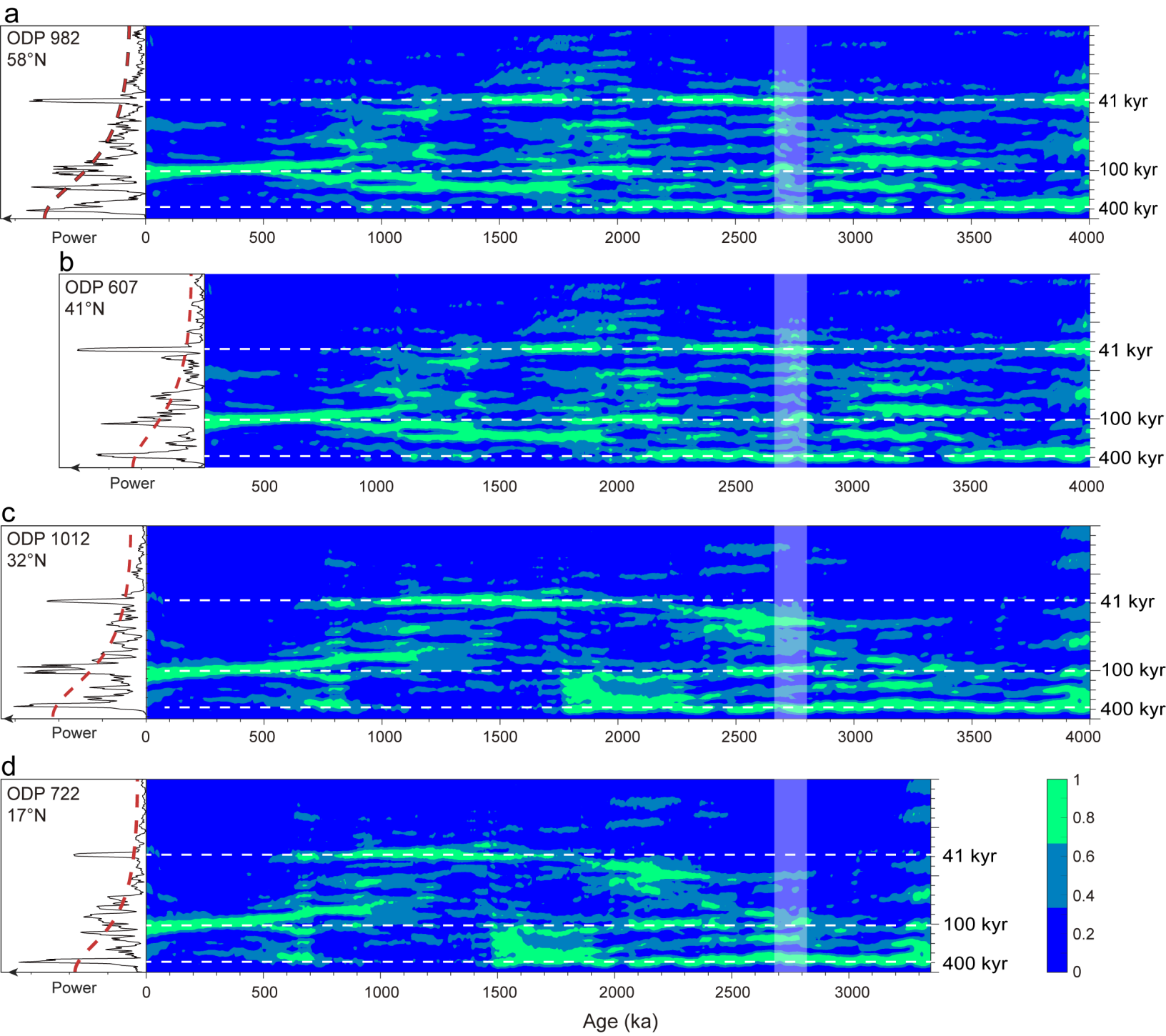
a
ODP 982
58°N
41 kyr
100 kyr
400 kyr
Power
0
500
1000
1500
2000
2500
3000
3500
4000
b
ODP 607
41°N
41 kyr
100 kyr
400 kyr
Power
500
1000
1500
2000
2500
3000
3500
4000
c
ODP 1012
32°N
41 kyr
100 kyr
400 kyr
Power
0
500
1000
1500
2000
2500
3000
3500
4000
d
ODP 722
17°N
41 kyr
100 kyr
400 kyr
Power
0
500
1000
1500
2000
2500
3000
1
0.8
0.6
0.4
0.2
0
Age (ka)

Figure 4.

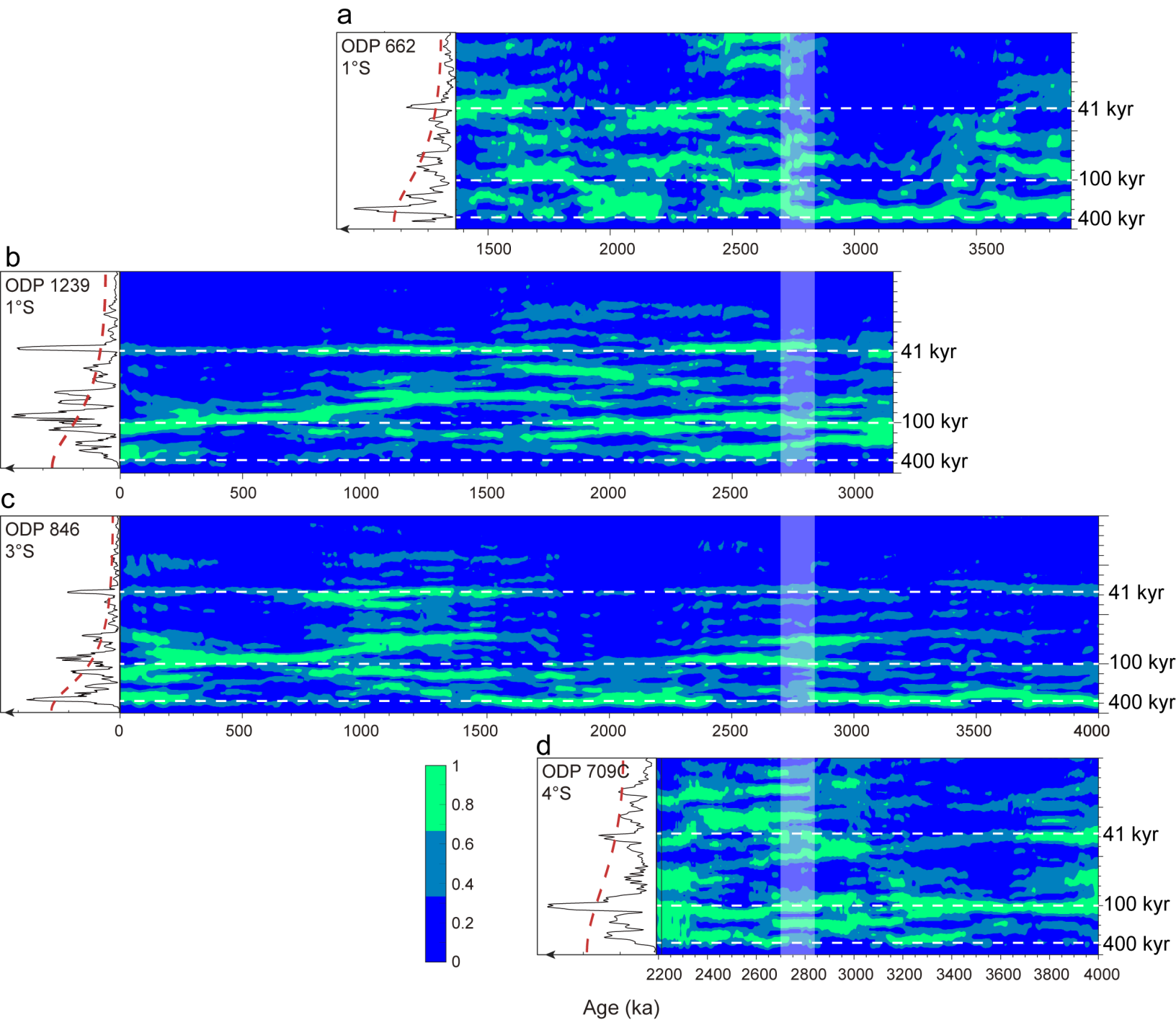
a
ODP 662
1°S
41 kyr
100 kyr
400 kyr
1500
2000
2500
3000
3500
b
ODP 1239
1°S
41 kyr
100 kyr
400 kyr
0
500
1000
1500
2000
2500
3000
c
ODP 846
3°S
41 kyr
100 kyr
400 kyr
0
500
1000
1500
2000
2500
3000
3500
4000
1
0.8
0.6
0.4
0.2
0
d
ODP 709C
4°S
41 kyr
100 kyr
400 kyr
2200
2400
2600
2800
3000
3200
3400
3600
3800
4000
Age (ka)

Figure 5.

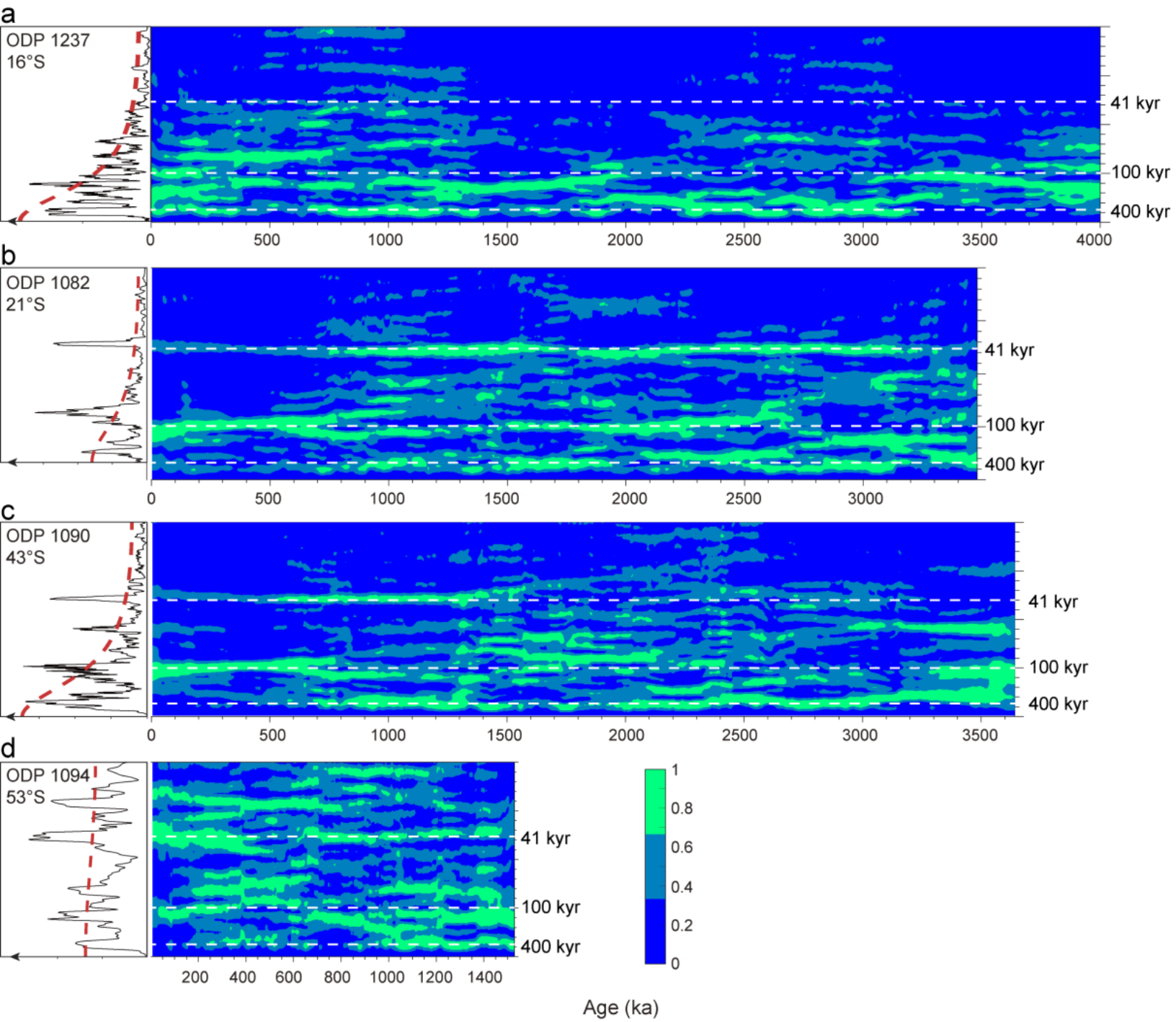
a
ODP 1237
16°S
41 kyr
100 kyr
400 kyr
0
500
1000
1500
2000
2500
3000
3500
4000
b
ODP 1082
21°S
41 kyr
100 kyr
400 kyr
0
500
1000
1500
2000
2500
3000
c
ODP 1090
43°S
41 kyr
100 kyr
400 kyr
0
500
1000
1500
2000
2500
3000
3500
d
ODP 1094
53°S
41 kyr
100 kyr
400 kyr
200
400
600
800
1000
1200
1400
1
0.8
0.6
0.4
0.2
0
Age (ka)

Figure 6.

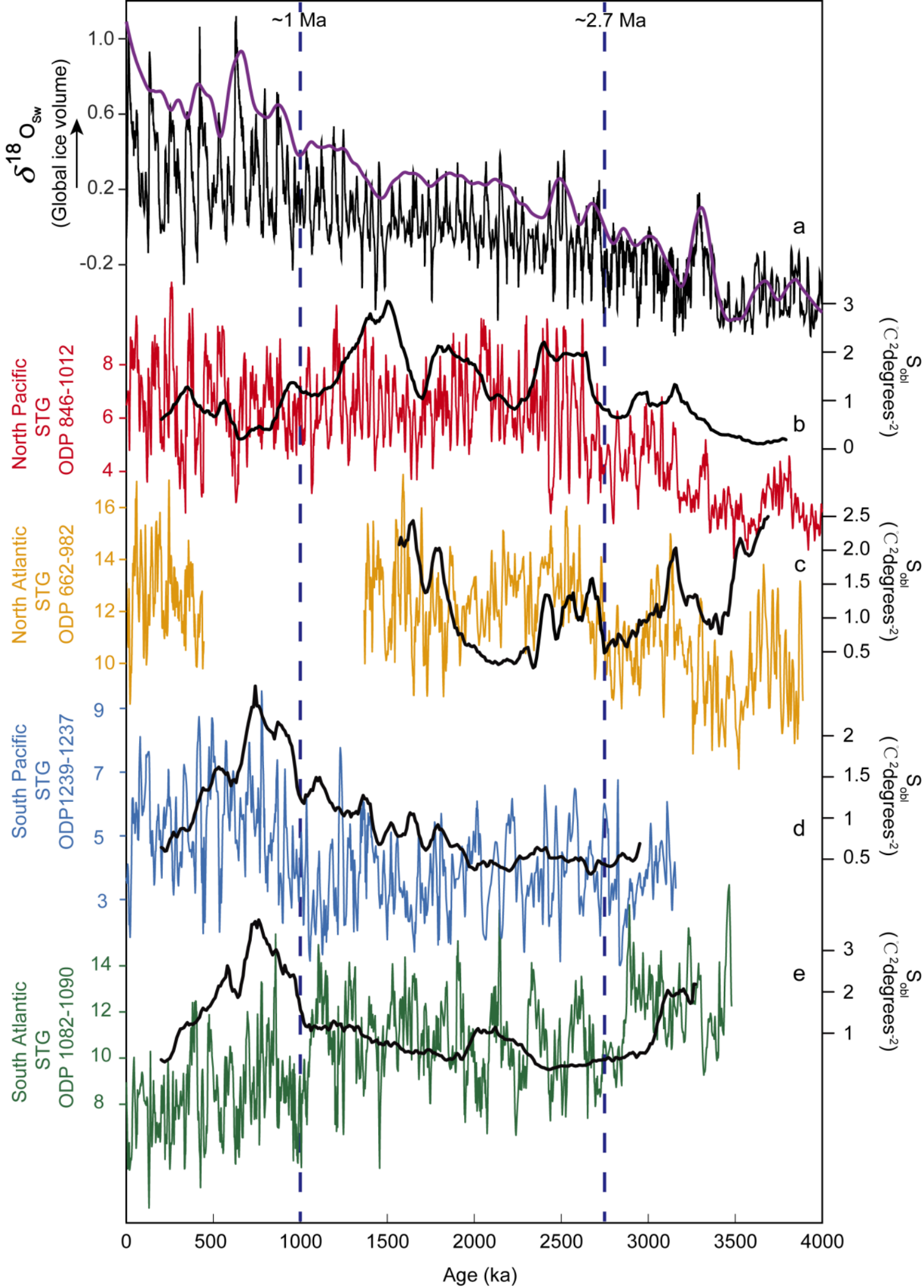
~1 Ma
~2.7 Ma
δ18Osw
(Global ice volume)
1.0
0.6
0.2
-0.2
a
North Pacific
STG
ODP 846-1012
8
6
4
b
3
2
1
0
Sobl
(°C2degrees-2)
North Atlantic
STG
ODP 662-982
16
14
12
10
c
2.5
2.0
1.5
1.0
0.5
South Pacific
STG
ODP1239-1237
9
7
5
3
d
2
1.5
1
0.5
South Atlantic
STG
ODP 1082-1090
14
12
10
8
e
3
2
1
0
500
1000
1500
2000
2500
3000
3500
4000
Age (ka)

Figure 7.

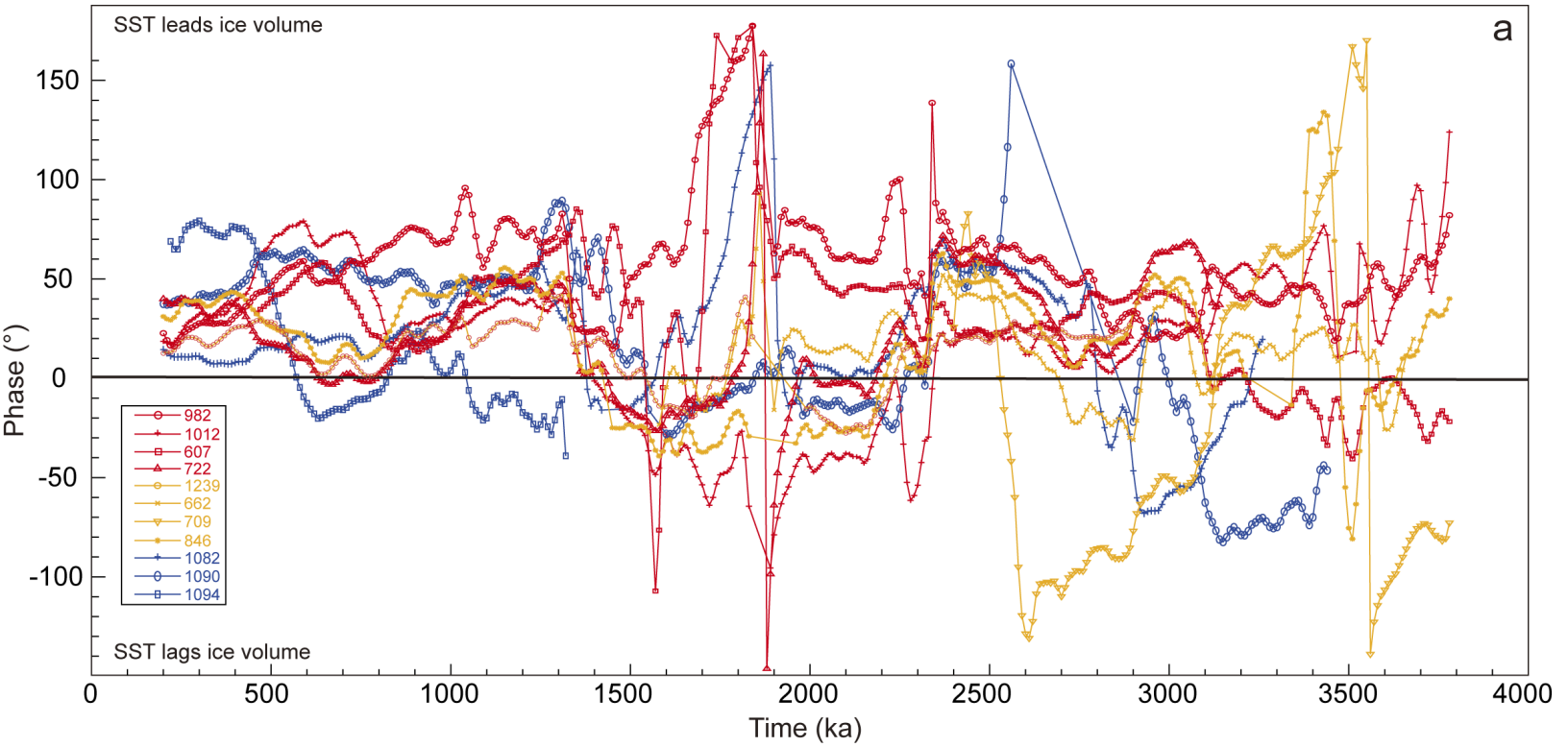
SST leads ice volume
a
Phase (°)
150
100
50
0
-50
-100
982
1012
607
722
1239
662
709
846
1082
1090
1094
SST lags ice volume
0
500
1000
1500
2000
2500
3000
3500
4000
Time (ka)

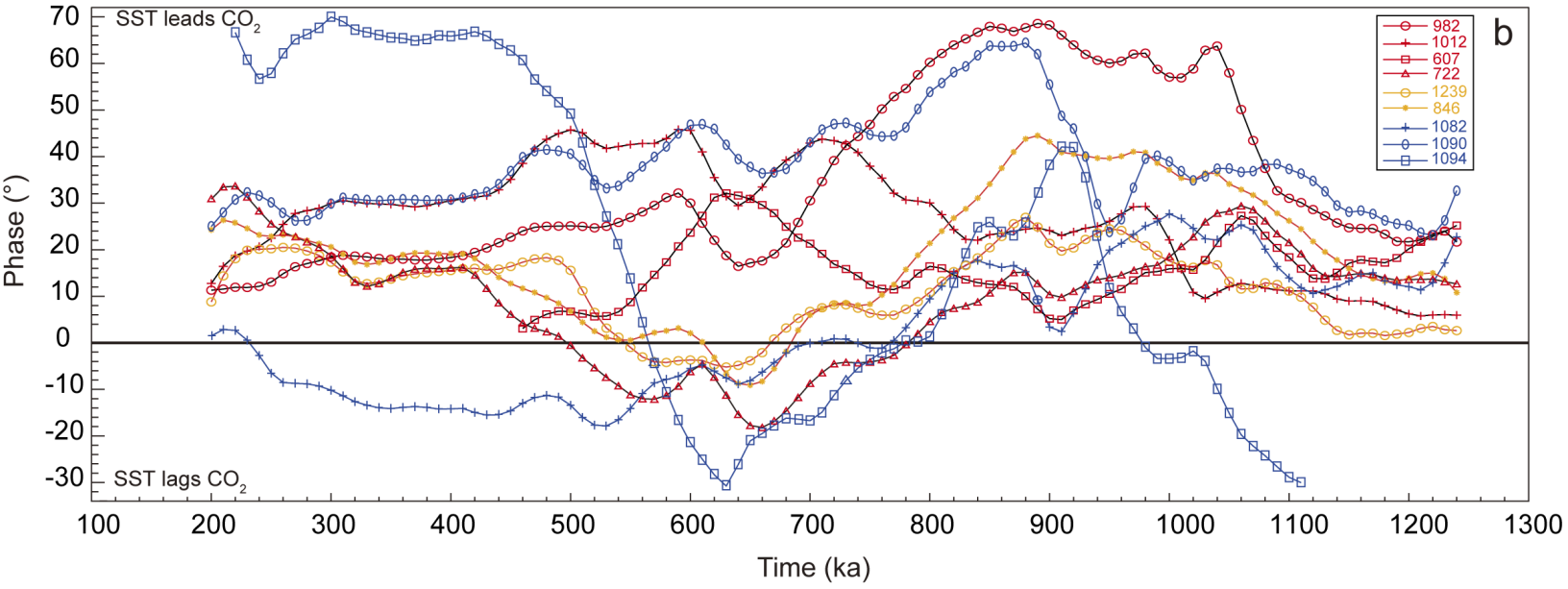
SST leads CO2
b
Phase (°)
70
60
50
40
30
20
10
0
-10
-20
-30
982
1012
607
722
1239
846
1082
1090
1094
SST lags CO2
100
200
300
400
500
600
700
800
900
1000
1100
1200
1300
Time (ka)

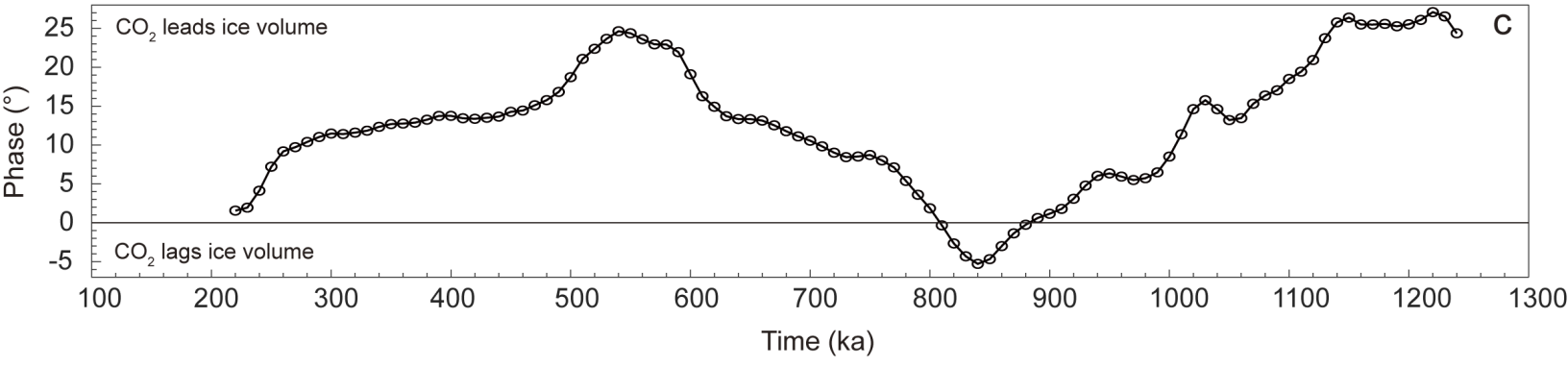
CO2 leads ice volume
c
Phase (°)
25
20
15
10
5
0
-5
CO2 lags ice volume
100
200
300
400
500
600
700
800
900
1000
1100
1200
1300
Time (ka)

Figure 8.

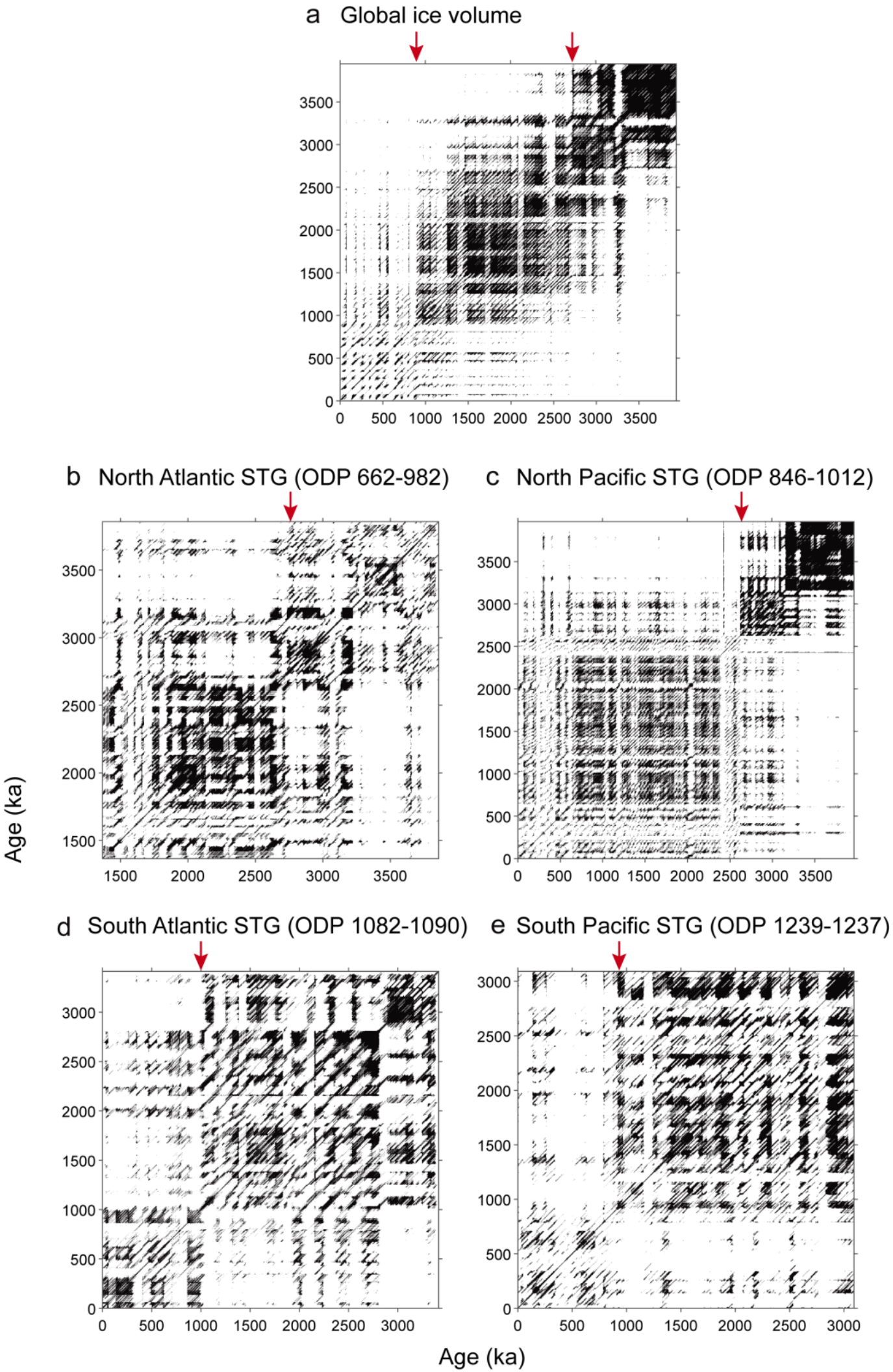
a Global ice volume
b North Atlantic STG (ODP 662-982)
c North Pacific STG (ODP 846-1012)
d South Atlantic STG (ODP 1082-1090)
e South Pacific STG (ODP 1239-1237)
Age (ka)
Age (ka)